4-3-2020

Determining improvements in Landsat spectral sampling for inland water quality monitoring

Ryan T. Ford
Rochester Institute of Technology

Anthony Vodacek
Rochester Institute of Technology

Recommended Citation
Ford, Ryan T., and Anthony Vodacek. "Determining Improvements in Landsat Spectral Sampling for Inland Water Quality Monitoring." Science of Remote Sensing, Elsevier, 3 Apr. 2020, doi.org/10.1016/j.srs.2020.100005.

Science of Remote Sensing 1 (2020) 100005

Contents lists available at ScienceDirect

Science of Remote Sensing

journal homepage: www.journals.elsevier.com/science-of-remote-sensing

Full Length Article

Determining improvements in Landsat spectral sampling for inland water quality monitoring

Ryan T. Ford *, Anthony Vodacek

Chester F. Carlson Center for Imaging Science, Rochester Institute of Technology, Rochester, NY, USA

ARTICLE INFO

Keywords:
Remote sensing
Landsat
Spectral sampling
Lakes
Cyanobacteria
Water quality monitoring

ABSTRACT

Inland waters are optically complex and provide an ongoing challenge to effective water quality monitoring through remote sensing. Imaging satellites with spectral sampling designed for this task often have coarse spatial resolutions, preventing any capture of information from small lakes. Medium resolution satellite systems such as Landsat 8 have the appropriate spatial resolution and sensitivity required to resolve these waterbodies, but the spectral sampling is not optimal. This work uses system simulation to explore potential changes to Landsat spectral sampling to determine if its ability to monitor inland waters could be improved. The HydroLight and MODTRAN radiative transfer models are used for simulation in a Look Up Table and spectrum matching approach to provide maximum flexibility intesting spectral sampling scenarios. To isolate the testing to the impacts of spectral sampling, all simulations were performed based on the known system noise characteristics of Landsat 8. Spectral sampling changes tested include the addition of yellow and red edge spectral bands as well as conversion to an imaging spectrometer. Simulated spectra of inland waters undergoing a cyanobacteria bloom, including atmospheric effects and sensor noise, were implemented with the Look-Up-Table retrieval process to extract estimated concentrations of waterbody components. The retrieval accuracy of each potential system is compared to that of a modeled Landsat 8 baseline. All potential systems show an increase of retrieval accuracy over the baseline. The best performing system design is an imaging spectrometer, followed by the addition of both a yellow and red edge band simultaneously, and the addition of either band individually. Testing also demonstrates that resampling an imaging spectrometer with 20 nm spectral resolution to the Landsat 8 band responses produces outputs matching those available from Landsat 8. Our results indicate that future Landsat missions should aim to add as much spectral sampling as is feasible, while maintaining at least the same sensitivity. The minimum change to improve water quality monitoring capability is the addition of a red edge spectral band.

1. Introduction

Accurate monitoring of inland water quality is critical as issues such as eutrophication and harmful algal blooms increase (A and National Water Quali, 2017). In-situ methods of assessing water quality can provide highly accurate measurements but are costly when implementing a spatially comprehensive analysis. In this regard, remote sensing has proven to be an effective tool for water quality monitoring over large spatial scales such as ocean continental margins (Gordon et al., 1983; O'Reilly et al., 1998; Lee et al., 2002; Carder et al., 2004; Hu et al., 2012). Passive imaging satellites have shown robust performance in monitoring clear oceanic waters but are at a disadvantage when monitoring optically complex waters (Ruddick et al., 2000; Gons et al., 2002; Gitelson et al., 2007; Palmer et al., 2015a; Kuhn et al., 2019). Optical complexity arises from interaction between the variable absorptive and scattering components of the water. Algorithms implemented in water quality monitoring often explicitly or implicitly utilize these inherent optical properties (IOPs) in analysis (Simis et al., 2005; Lunettaa et al., 2015; Kutser et al., 2016; Zheng and DiGiacomo, 2017; Li et al., 2018), attempting to appropriately parse and attribute the contribution of waterbody components to the measured signal. Given the spectral dependence of these mixtures of IOPs, the algorithm performance is dependent on the spectral sampling and spectral resolution of the imaging system.

By examining needs for coastal and inland remote sensing, several studies have determined that current satellite missions (e.g. MODIS, MERIS, & VIIRS) are suboptimal and recommended increased spectral sampling and spectral resolution for future sensors (Palmer et al., 2015b;

* Corresponding author.
E-mail address: rmf3259@rit.edu (R.T. Ford).

https://doi.org/10.1016/j.srs.2020.100005
Received 12 September 2019; Received in revised form 13 December 2019; Accepted 19 December 2019
Available online 3 April 2020

Mouw et al., 2015; Dekker et al., 2018; IOCCG, 2018). Sensors with better spectral resolution and spectral sampling improve atmospheric compensation (IOCCG, 2012), enable cross validation and vicarious calibration of multi-platform data (Pahlevan et al., 2019), and allow better leveraging of spectral features in algorithms. Imaging satellites designed for ocean color applications, such as MODIS and OLCI aboard Sentinel-3, have a more desirable spectral resolution and spectral sampling, however they are limited by their coarse spatial resolution to observing large inland lakes. A 300 m spatial resolution such as that on OLCI can resolve ~60% of global lake area (IOCCG, 2018).

Medium spatial resolution sensors (10–30 m) designed for terrestrial mapping are capable of resolving ~90% or more of global lake area (IOCCG, 2018) and their radiometric sensitivity has been improving with advancing technology. Landsat 8 has been applied to inland water monitoring due to increased spectral sampling and radiometric performance advances over its predecessors (Vanhellemont and Ruddick, 2014; Kutser et al., 2016; Li et al., 2018). The next incarnation of the Landsat mission, Landsat 9, is slated to copy the existing architecture of Landsat 8 and will transmit 14-bit data to ground (Wulder et al., 2019). NASA and the USGS are in the process of determining specifications for Landsat 10. Additional improvements to spectral resolution and spectral sampling of Landsat sensors should enhance monitoring of complex inland waterbodies (Dekker et al., 2018). However, the potential risk of augmented spectral sampling affecting Landsat data continuity must be considered and the benefits of additional spectral resolution and spectral sampling should be investigated (Recommendations for, 2018).

In this study we model the end-to-end imaging chain to understand how augmenting the spectral sampling and spectral resolution of future Landsat missions could benefit their use for inland water quality monitoring. Our model includes potential Landsat systems spectral sampling and spectral resolution, system noise, and a modeled atmosphere. Our use case target is modeled water-leaving radiance of cyanobacteria blooms propagated to the sensor. We then model the atmospheric compensation process and implement the Look-Up-Table (LUT) approach of Concha and Schott (2016) to retrieve the concentrations of four optically active components, Chlorophyll-a (Chl), Total Suspended Solids (TSS), Colored Dissolved Organic Matter (CDOM), and Phycocyanin (PC). The accuracy of the retrieved concentrations is used to determine the most effective spectral sampling and spectral resolution.

For a potential multispectral Landsat sensor this process is used to evaluate how adding a yellow band and a red edge band to the existing suite of Landsat bands affects the retrieval task. A yellow band is of interest for several reasons. Landsat 8 spectral sampling has a gap in this region and adding a yellow band provides nearly complete spectral sampling in the visible spectrum. Further the PC absorption maximum is in the yellow and algorithms for retrieving PC have been developed for sensors with this band such as MERIS (Schalles and Yacobi, 2000; Simis et al., 2007; Mishra and Mishra, 2014). Finally, other sensors in addition to MERIS have spectral bands in the yellow such as DigitalGlobe's WorldView-2 and -3 sensors as well as Sentinel-3 and the planned water quality focused Harmful Algal Bloom Satellite-1 (HABsat-1) cubesat constellation (Donlon et al., 2012; Johansen et al., 2019). A red edge band has wide application in terrestrial remote sensing community. In a survey of Landsat data user needs, a majority of users indicated that a red edge band would allow for a significant improvement of data effectiveness in their application area (Wu et al., 2019). A red edge band is also useful in remote sensing of coastal and inland waters which often have non-negligible amounts of reflectance signal in the NIR region. Further, lack of a band in this spectral region has shown to be limiting in the application of Landsat for inland water remote sensing (Kutser et al., 2016).

For a potential Landsat imaging spectrometer, this process is used to determine the impact of spectral sampling and spectral resolution on the retrieval task as well as an assessment of continuity with historical Landsat data. The transition of Landsat to a full imaging spectrometer was indicated to be the optimal need in spectral resolution by Landsat data users (Wu et al., 2019). The spectral sampling and coverage of imaging spectrometers are indicated to be desirable by the water remote sensing community (Dekker et al., 2018). Because an imaging spectrometer would be a large departure from the historic Landsat spectral sampling and resolution, we test the impact of resampling an imaging spectrometer to historical Landsat multispectral bands to assess data continuity.

2. Methods

2.1. Modeling process overview

To test the potential of different Landsat system designs for component mapping we model the end-to-end retrieval process in full, beginning with the sun's light energy interacting with the water to create the water leaving radiance and ending with the retrieval of component concentrations. The first step of this process is generating a modeled set of test water leaving radiance spectra using the EcoLight package of HydroLight (Mobley and Sundman, 2013). HydroLight is an in-water radiative transfer model that solves a one-dimensional radiative transfer equation and outputs the radiance at discrete depths within the water column, as well as the water leaving radiance over a discretized hemisphere. The EcoLight package performs this computation only for a nadir viewing angle, decreasing computation time. EcoLight also simulates effects of the water surface on the generated radiance spectra, including glint and wave shape, but does not include wave shadowing or white caps. The component concentrations and IOPs input to EcoLight are randomly selected from a range of values to create the test pixel radiance spectrum. Atmospheric effects are then added using the MODTRAN radiative transfer code (Berk et al., 1989). This test pixel radiance is then spectrally sampled using the Relative Spectral Response (RSR) of the Landsat 8 bands as well as modeled RSRs, both of which include noise and quantization effects based on known Landsat 8 band characteristics.

Once the scene is modeled through the sensor, the same MODTRAN data are used to remove the atmospheric effects. This would seem to imply a perfect atmospheric compensation, however the compensation is not perfect due to the spectral sampling process, the signal dependent sensor noise, and quantization. A spectral matching algorithm, akin to the work of Mobley et al., (2005), Gerace et al. (2013), and Concha and Schott (2016), is then implemented to determine component concentrations by comparing the test pixel radiance spectra to LUT entries. LUTs of modeled water leaving radiance spectra are also generated using EcoLight. Each entry of the LUT corresponds to a pre-defined set of component concentrations covering an expected range of values. The randomly generated test pixel spectra are first matched to a best-fit LUT entry and then a process of interpolation and minimization results in a final retrieval. The retrieved concentrations are then compared to the test pixel concentrations to determine the retrieval error. These processes are described in more detail in Sections 2.2 - 2.7.

2.2. Test pixel and Look-Up-Table generation

In this work, both the randomly generated test pixels as well as the structured LUTs were generated using the EcoLight radiative transfer model. EcoLight uses the IOPs of each of the optically active components in the water to output a spectral water leaving radiance between 400 nm and 900 nm at 5 nm increments. In this case five components were considered, pure water, Chl, TSS, CDOM, and PC. This work used the freshwater absorption spectrum of Pope and Fry (1997) and the freshwater scattering spectrum of Morel et al. (1974), both of which are built into EcoLight. The Chl, TSS, and PC components require inputs of concentrations, mass specific absorption and scattering spectra, and scattering phase functions. The specific scattering spectrum for Chl and for TSS were taken from Bukata et al. (1991) and a PC scattering spectrum was determined by subtracting the Chl spectrum from a measurement of specific scattering by cyanobacteria cells collected by Ahn et al. (1992).

Table 1
Component concentrations used to generate the retrieval LUT.

Chlorophyll-a (mg/m^3)	Total Suspended Solids (g/m^3)	CDOM (1/m)	Phycocyanin (mg/m^3)
10.0	3.0	0.1	25.0
50.0	10.0	1.00	50.0
75.0	17.0	2.5	75.0
125.0	25.0		125.0
175.0			140.0

Although a single scattering spectrum was used, two Fournier-Forand phase scattering functions (Fournier and Forand, 1994), whose shape depends on the ratio of backscattering to total scattering, were used to describe the angular dependence of scattering for the non-water components. The ratio values chosen were 1.8% and 2.0%, measured in harbor waters by Petzold (1972) and the mean ratio reported in the Oslo Fjord by Aas et al. (2005), respectively. Each component is represented by three values of specific absorption, or absorption in the case of CDOM. This was to represent the variability of specific absorption spectra reported in the literature (Vodacek et al., 1997; Fujiki and Taguchi, 2002; Stramski et al., 2007; Mishra et al., 2013). Two PC absorption spectra were taken from samples of a 2017 cyanobacteria bloom in Honeoye lake, located in the Finger Lakes region of New York state. PC was extracted and quantified using the freeze-thaw method of Sarada et al. (1999). The third PC absorption spectrum with a value of 0.005 mg/mˆ3 at 620 nm was taken from measurements by Mishra et al. (2013) of Mississippi ponds. The three absorption spectra for Chl, TSS, and CDOM were obtained from the measurements of Nguy-Robertson et al. (2013) from lakes and reservoirs in Indiana bracketing the range of variability they reported. The set of 1000 random test pixels and the structured retrieval LUT were built using these IOP spectra. Both the test data set and structured LUT use the same IOPs to replicate the methods of Gerace et al. (2013) and Concha and Schott (2016) where IOPs measurements were collected simultaneous with imagery and therefore known, excluding any measurement error. EcoLight uses RADTRAN to determine the scene irradiance, thus requiring date (September 16), time (16 GMT), and location (Lat/Long 42.83 N/77.7 W). These values corresponded to the cyanobacteria bloom season and time of day for a Landsat 8 overpass corresponding to western New York.

Concentrations for each of the test pixels were chosen randomly from preset ranges. These ranges were 10–150 mg/m^3 for Chl, 25–120 mg/m^3 for PC, 3–20 g/m^3 for TSS, and 0.1 to 2.0 m^{-1} for CDOM. These values were chosen based on measured concentration ranges reported in the literature during cyanobacteria blooms (Randolph et al., 2008; Mishra et al., 2013; Yacobi et al., 2015). The water column is assumed to be optically thick with no bottom effects, simulated through use of the "infinitely deep water" option in EcoLight. One of the three absorption spectra and one the of two scattering phase functions were randomly chosen for each run. Note that the generated test pixel data are spectral and will be resampled to modeled sensor RSRs. The same scattering, absorption, and phase scattering data were used for generation of the LUT in a structured fashion. Discrete concentration levels for each component were used in the LUT. A full list of concentration levels is shown in Table 1. The highest component concentration levels in the LUT were chosen to be greater than those for the test pixels. The LUT entries are spectral and will be resampled to modeled sensor RSRs. Based on the concentrations listed in Table 1, three possible specific absorption spectra for each of the four absorbing components, a single specific scattering spectrum for each component, and two scattering phase functions, the LUT contains 48,600 entries.

2.3. Addition of atmospheric effects

$$L_{sens} = L_W * t_{atmo} + L_{atmo} \quad (1)$$

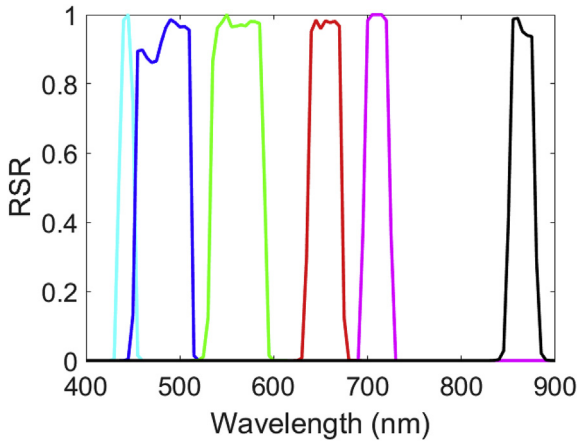

Fig. 1. Spectral sampling of Landsat 8 with an added Super-Gaussian red edge band centered at 720 nm (pink). (For interpretation of the references to color in this figure legend, the reader is referred to the Web version of this article.)

The radiative transfer model MODTRAN was used to model the spectral atmospheric transmission and upwelled radiance (Berk et al., 1989). Consistent with EcoLight, these effects were modeled for nadir view from ground to the sun synchronous altitude of Landsat 8 (705 km) and the date, time, and latitude/longitude were set to be the same as used for generation of the test pixels and LUT. The rural aerosol profile with a 23 km visibility was used with at mid-latitude summer model atmosphere. This visibility represents clear sky low haze conditions for ground viewing from space. This MODTRAN output for spectrally dependent atmospheric transmission (t_{atmos}) and radiance (L_{atmos}) is combined with the water leaving radiance spectra (L_W) to form the sensor reaching spectral radiance (L_{sens}) using Equation (1). After the addition of atmospheric effects, the test pixel radiance is resampled to the RSR of the system being tested, described in section 2.4.

The retrieval process requires atmospheric compensation of the spectra. This compensation is done by using the same MODTRAN output and Equation (2), where the atmospheric values have been sampled to the spectral bands of the imaging system being modeled using the real and modeled RSRs described in Section 2.4.

$$L_{ret}' = \frac{L_{sens}' - L_{atmo}'}{t_{atmo}'} \quad (2)$$

As previously stated, this compensation routine assumes perfect knowledge of the atmosphere which is generally not the case due to the complexity of determining atmospheric variables. This assumption is to allow atmospheric effects to have an impact on the simulated radiance spectra, namely through the process of spectral sampling (Section 2.4), adding noise, and quantization (Section 2.5), without the residual error obfuscating the impacts of the tested spectral sampling and resolution configurations which are the focus of this study. Reducing error from imperfect atmospheric compensation is an ongoing problem critical to water quality remote sensing that still requires study.

2.4. Spectral sampling and spectral resolution

With our focus on investigating spectral resolution and spectral sampling for future Landsat missions, we modeled Landsat as a multispectral system and as an imaging spectrometer. For a future multispectral system, we used the Landsat 8 RSRs and additional spectral bands modeled as Super-Gaussians, described in equation (3).

$$RSR_{modeled} = e^{-\left(\frac{\lambda-\lambda_{center}}{w}\right)^{10}} \quad (3)$$

Where λ_{center} represents the center wavelength and w is the approximate

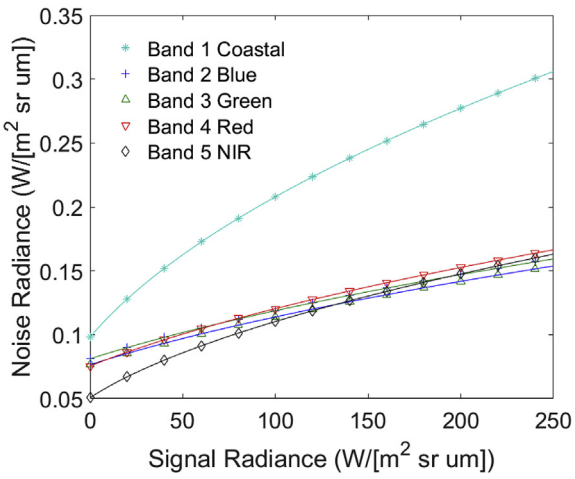

Fig. 2. The output Noise Radiance versus the input Signal Radiance of the first 5 Landsat 8 bands based on the model by Morfitt et al. (2015).

half-width half-max (HWHM) which we use to report bandwidth for most cases in this work. We will explicitly state the use of full-width half-max (FWHM) where appropriate. These functions approximate the RSR of the existing Landsat bands by having a level spectral response over across the center wavelength and a sharp fall-off outside of it. As an example, Fig. 1 shows the RSR of a modeled band centered at 720 nm (red edge) along with the RSRs of bands one through five of Landsat 8. We test multiple bands, with band centers ranging from 590 nm to 630 nm for the yellow and 675 nm–725 nm for the red edge both in 1 nm increments. The approximate HWHMs of all bands ranged from 15 to 30 nm wide (FWHMs 30 nm–60 nm) which are similar to the existing Landsat 8 bands. We also test how adding both a yellow and red edge band simultaneously affect retrieval. For the simultaneous test, band centers range from 590 nm to 630 nm for the yellow and 680 nm–725 nm both in 5 nm increments. The HWHMs are 15 nm, 18 nm, 20 nm, 25 nm, and 30 nm for both bands.

For a future imaging spectrometer, we tested systems with 5 nm FWHM and FWHMs between 10 nm and 100 nm at 10 nm increments (see Fig. 8) in the range of 400–900 nm. In each case, the center of the shortest wavelength band is 400 nm. The approximate HWHM of the bands were chosen to be the point where an adjacent band's approximate HWHM overlaps (e.g. a system with 20 nm FWHM would have bands with an approximate HWHM of 10 nm). In a second test of band center locations, spectrometers with 20 nm, 40 nm, 60 nm, and 80 nm FWHM were incrementally shifted to determine how changing placement would affect retrieval. For each system, band centers were shifted by 5 nm increments until the wavelength repeated. For example, a system that had 20 nm spacing would be tested with the location of its shortest wavelength band center at 400, 395, 390, 385 nm (shifts of 0, 5, 10, and 15 nm). If the band centers where shifted another 5 nm it would return the sampling to that of the original system. The 20 nm system was also used to test how well a spectrometer could be resampled to the historic Landsat product for data continuity. This was done by modeling a 20 nm spectrometer, resampling its retrieved radiances to Landsat 8 RSRs, and using the resampled spectra in the constituent retrieval process. In this data continuity test, the band center locations were also shifted by 5, 10, and 15 nm.

2.5. System noise

System noise for the existing Landsat 8 bands was implemented in the modeling chain using the noise model from Morfitt et al. (2015). As shown in Equation (4), this model determines the total noise radiance (N), with units W/(m^2 sr μm), using the quantization noise coefficient (q), the signal-independent noise coefficient (a), the signal dependent noise coefficient (b), the scene radiance (S), and a factor of 0.8 to account for error reduction from the cubic convolution resampling of the Level-1 Product. The values for a, b, and q are band specific and were generated using on-orbit Landsat 8 noise measurements. This noise is added to the signal of each band as the standard deviation of a zero mean normally distributed value. The noise radiance per signal radiance is shown in Fig. 2.

$$N = \sqrt{0.8\left(\sqrt{b^{*}S + a}\right)^{2} + q^{2}} \tag{4}$$

Since we want to determine the most effective spectral sampling and spectral resolution, we also need a process to estimate the effect of band position and HWHM on the noise of the modeled spectral bands for both the multispectral and imaging spectrometer cases. To model the noise of a given band center we interpolate from the Landsat 8 bands and then adjust based on the modeled band HWHM, allowing us to test different sensor configurations. For example, for a modeled band at 620 nm with a HWHM of 20 nm we interpolate the noise and HWHM of Landsat bands 3 (center – 561 nm, HWHM – 28.5 nm) and 4 (center – 654 nm, HWHM – 18.5 nm) at 620 nm producing the noise for a band with a HWHM of 22.1 nm. The noise of the modeled band is then multiplied by the ratio of the interpolated width to its desired width, thus narrower bands have more noise and wider bands have less. With this process the signal dependent and independent noise are implicitly included. The sampled radiance spectra are then entered in the component retrieval process.

2.6. Constituent retrieval

Following the procedures in sections 2.3 through 2.5 the test pixels have the qualities of real data (atmospheric effects, spectral resampling, system noise) and have undergone atmospheric compensation thus are prepared for constituent retrieval using the LUT and spectral matching process. The LUT of radiance spectra is also sampled to the modeled system RSRs. The root-mean-square-error (RMSE) between each LUT entry and each test pixel is determined using equation (5) where N is the number of bands in the system while the subscripts test and LUT refer to the test pixel and LUT spectra, respectively. The lowest root mean square error is used to identify the most similar LUT spectrum and its IOPs.

$$RMSE = \sqrt{\frac{\sum_{i=0}^{N}\left(\vec{L}_{test} - \vec{L}_{LUT}\right)^{2}}{N}} \tag{5}$$

As the LUT entries are discretely spaced, we perform an interpolation of component concentrations to improve the accuracy of retrieval. Like the interpolation process by Concha and Schott, we perform an interpolation of LUT component concentrations and LUT water-leaving radiance spectra to build a linear function that approximates the water-leaving radiance spectrum of any given set of concentrations. This interpolation uses only LUT entries that have the same IOP set as the most similar LUT spectrum determined from equation (5), as we assume that these are the IOPs that best represent the test pixel. Unlike Concha and Schott who only considered three optically active components (Chl, TSS, CDOM), we consider a fourth (PC) and therefore interpolate across 4 components instead of 3. The input concentrations that minimize the difference between the approximated spectrum and the test pixel spectrum are determined using a nonlinear least-squares fitting algorithm from MATLAB (Mathworks, 2017) where the concentrations of the most similar LUT spectrum are used as the initial guess. The concentrations output by the minimization are recorded as the retrieved concentrations for each of the 1000 test pixels.

2.7. Error reporting

Error in the concentration retrieval has several sources beyond our target of spectral sampling including noise in the overall process, IOPs

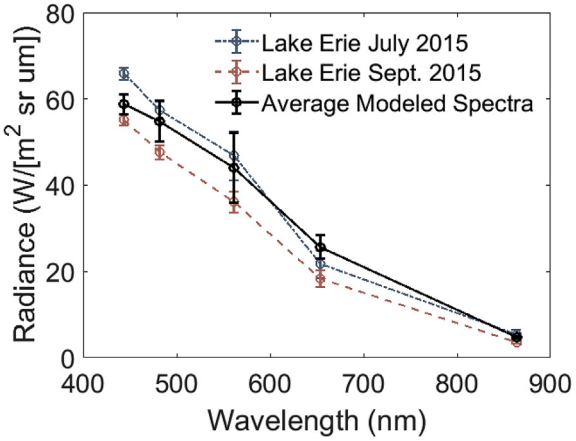

Fig. 3. Modeled Top of Atmosphere Radiance compared to TOA radiance from Landsat 8 Imagery over Lake Erie in 2015. Blue is data taken from a July image while red is data taken from a September image. (For interpretation of the references to color in this figure legend, the reader is referred to the Web version of this article.)

used, and the LUT search and interpolation process. This experiment is designed and reported in a way that changes in error are driven by changes in spectral sampling. Error in retrieval is reported as Normalized Root Mean Square Error (NRMSE). This value is equivalent to root mean square error but normalized by the difference between highest and lowest concentration present within the test pixel set. Equation (6) describes the NRMSE, where N in this case is the number of test pixels, the *ret* and *truth* subscript indicate the retrieved concentration and truth concentration respectively, and max/min represent the maximum and minimum concentrations of the test pixel set. The goal of this work is to determine improvement over Landsat 8 spectral sampling and NRMSE allows consistent comparison of performance across components and system designs.

$$NRMSE = \frac{\sqrt{\frac{\sum_{i=0}^{N}(C_{ret} - C_{truth})^2}{N}}}{C_{max} - C_{min}} \tag{6}$$

3. Results and discussion

3.1. Comparison of modeled spectra to real data

As a simple test to verify our modeling process we compare the TOA radiance spectra of our test pixels to that of radiometrically calibrated Landsat 8 scenes containing cyanobacteria blooms. Two Landsat 8 images, collected in July and September 2015 (LC8019032015209LGN00 and LC8019032015257LGN00) over Lake Erie, were selected for comparison. A region of interest containing bloom and non-bloom waters north of Port Clinton, Ohio was selected by visual inspection. This region falls near a sampling site where the National Oceanic and Atmospheric Administration's Great Lakes Environmental Research Lab measure chlorophyll concentrations weekly each year, including between July and October of 2015 (Vander Woude et al., 2019). Concentrations at this site (WE15) ranged between 4 and 221 mg/m^3, agreeing well with our modeled range (NOAA, 2019). The region of interest mean radiance and its standard deviation for each band were calculated and compared against the mean and standard deviation of the 1000 test pixels which also represent bloom and non-bloom conditions, shown in Fig. 3.

In each band, the standard deviation radiance of the modeled spectra overlaps with the standard deviation radiance of at least one of the two images. It is expected that these spectra should be similar considering they are dominated by atmospheric radiance. Spectral differences may arise from IOP variability, random aspect of the test pixels, and the MODTRAN inputs used to generate the atmosphere. These results indicate the modeling process produces reasonably realistic spectra.

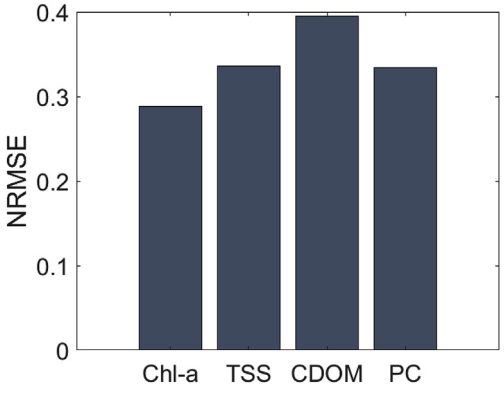

Fig. 4. Concentration retrieval NRMSE of a modeled system with the same spectral coverage and noise characteristics of Landsat 8.

3.2. Retrieval performance using Landsat 8 spectral sampling

We modeled the Landsat 8 system, using its spectral sampling and noise characteristics, to set a baseline of retrieval error against which other systems could be compared. We retrieved the water components from all 1000 modeled test pixels. Error was reported as NRMSE in Fig. 4.

3.3. The impact of additional multispectral bands

The results of modeled water constituent retrieval are provided in Fig. 5 for the addition of a yellow band, in Fig. 6 for the addition of a red edge band, and in Fig. 7 for the addition of both bands. For these three figures the NRMSE of the retrieved component varies as a function of band center and bandwidth allowing critical assessment of tradeoffs for these variables. Note that the color scales in each figure are not fixed to better visualize results.

The results in Fig. 5 indicate a yellow band with a HWHM in the range of 15 nm and 20 nm with a center around 625 nm leads to the greatest improvement in retrieval. The retrieval of Chl, TSS, and CDOM all outperform the baseline Landsat 8 system when a band is added with said properties. CDOM outperforms the base system at all locations regardless of band placement, an intuitive result as adding more spectral information should allow for better fitting of the observed spectra. Chl and TSS outperform the baseline system for the majority of tested bands except those closer to 590 nm. This degraded retrieval accuracy is likely a result of redundant information from the overlap of the modeled yellow band and the existing Landsat 8 green band causing confusion in the LUT retrieval process. This is most clearly illustrated by Chl, which shows retrieval error decrease faster for thinner bands as band centers increase from 590 nm.

PC retrieval is inconsistent relative to the other components. Furthermore, the range of band centers that perhaps show improvement over the baseline (605 nm–615 nm) are slightly removed from the PC absorption feature. This offset may allow the algorithm to better parse out the IOPs of PC from the other components in this region. Conversely this offset may help the retrieval algorithm better determine the IOPs of the other components and subsequently PC, however this is not supported by the reported retrieval errors of the other components in said region. Finally, the retrieval process may attribute noise in the spectrum to PC to better fit other components.

The retrieval results of the added red edge band show improvement comparable to that of the added yellow band, driven primarily by improvements in Chl and PC retrieval. These components show an improvement over the baseline system regardless of band placement and width. The retrieval error of Chl decreased significantly with the addition

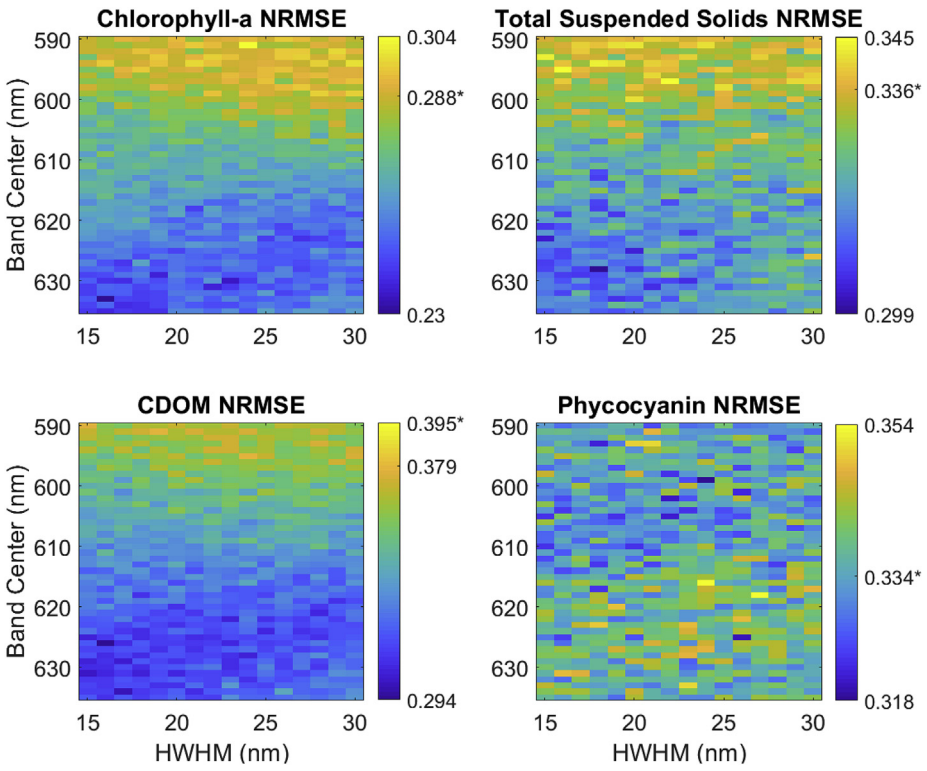

Fig. 5. Retrieval NRMSE for each component using modeled future Landsat systems with Landsat 8 spectral coverage and an added yellow band. Each graph represents a different component with the y-axis being the center of the added yellow band, the x-axis being the approximate HWHM, and the color axis being the NRMSE. The NRMSE scales for each component are variable to allow for better visualization. The retrieval NRMSE from the baseline Landsat 8 model (see Fig. 4) is labeled on the colorbar with an asterisk. (For interpretation of the references to color in this figure legend, the reader is referred to the Web version of this article.)

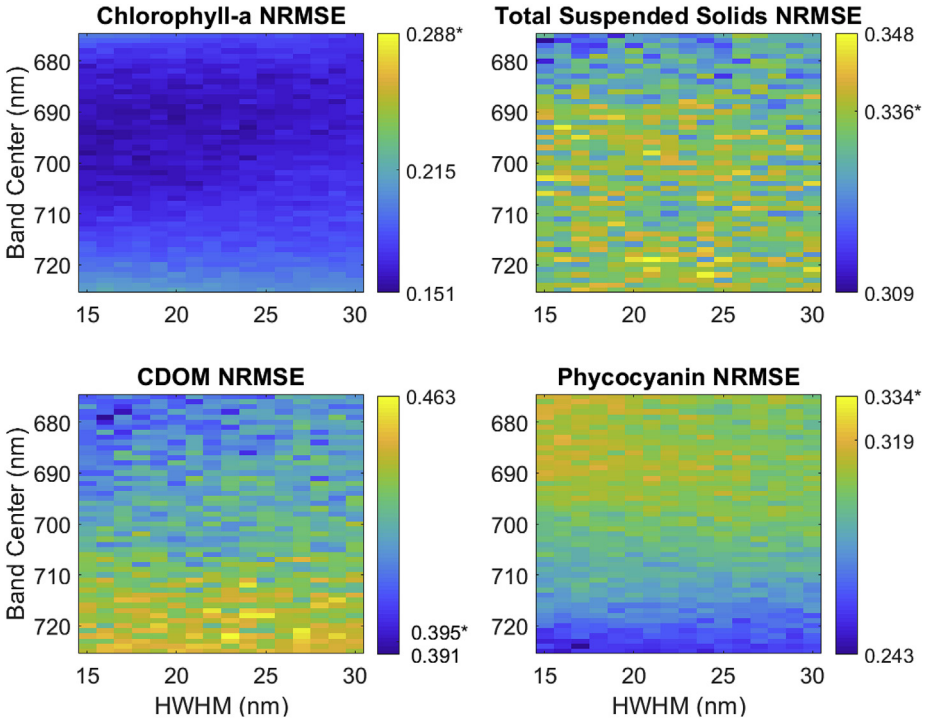

Fig. 6. Retrieval NRMSE for each component using modeled future Landsat systems with Landsat 8 spectral coverage and an added red edge band. Each graph represents a different component with the y-axis being the center of the added red edge band, the x-axis being the approximate HWHM, and the color axis being the NRMSE. The NRMSE scales for each component are variable to allow for better visualization. The retrieval NRMSE from the baseline Landsat 8 model (see Fig. 4) is labeled on the colorbar with an asterisk. (For interpretation of the references to color in this figure legend, the reader is referred to the Web version of this article.)

of the red edge band, as was expected based on its absorption minimum and fluorescence emission peak in this region (Mitchell and Kiefer, 1988; Bricaud et al., 1995). This result is encouraging considering that the placement of a red edge band would most likely be determined based on terrestrial application needs. The best Chl retrieval tends to favor band centers ranging from 690 nm to 705 nm, with an approximate HWHM around 15 nm–20 nm.

PC shows improvement with all possible red edge bands with the best retrievals taking place with band centers at the long wavelength end of the tested range. This may be caused by the methodology used to derive the mass specific scattering spectrum used for PC, which attributes most of the phytoplankton NIR scattering to the component containing PC (Ahn et al., 1992). This increased scattering has also previously been used as the basis for a remote sensing index-based algorithm for

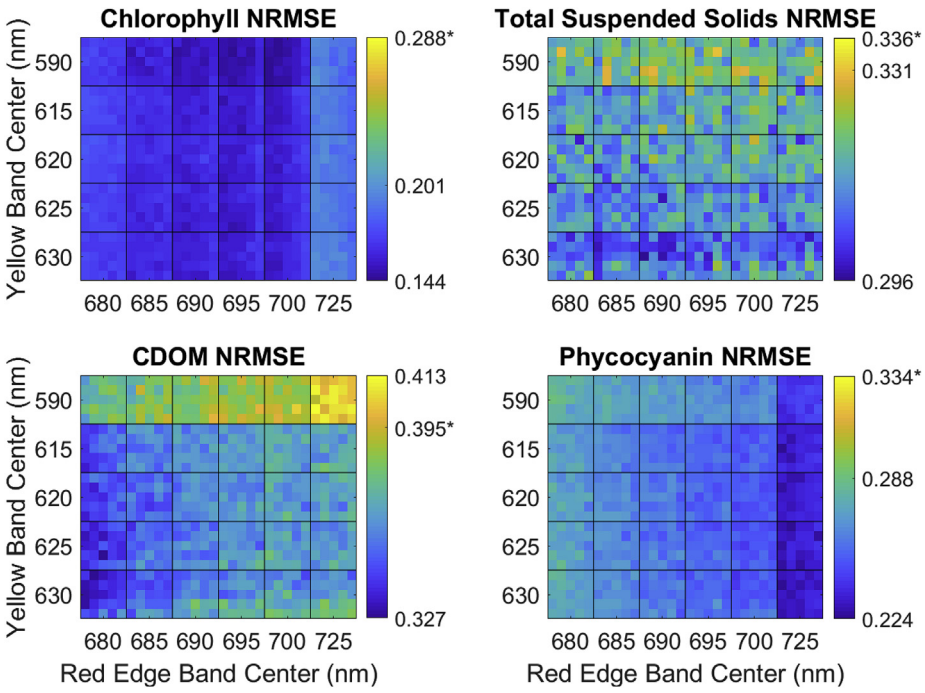

Fig. 7. Retrieval NRMSE for each component using modeled future Landsat systems with Landsat 8 spectral coverage and both an added Red Edge and Yellow band. Each graph represents a different component with the y-axis being the center of the added yellow band, the x-axis the center of the added Red Edge Band, and the color axis being the NRMSE. Each of the 30 large boxes represent a different band combination, with the sub-elements representing different HWHMs. The sub-elements represented HWHMs of 15, 18, 20, 25, and 30 nm from top to bottom for the yellow band and left to right for the Red Edge band. The NRMSE scales for each component are variable to allow for better visualization. The retrieval NRMSE from the baseline Landsat 8 model (see Fig. 4) is labeled on the colorbar with an asterisk. (For interpretation of the references to color in this figure legend, the reader is referred to the Web version of this article.)

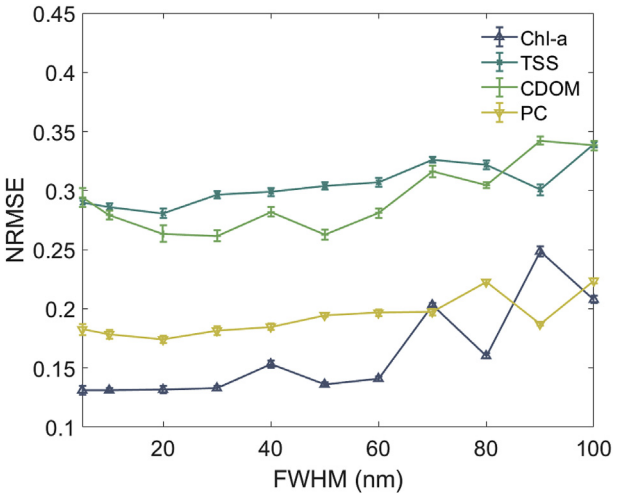

Fig. 8. NRMSE of retrieval for modeled imaging spectrometers with varying incrementing bandwidths. Retrieval error of each component is represented by a different line, where all lines show increasing error with increasing bandwidth.

monitoring cyanobacteria blooms known as the Cyanobacteria Index (Wynne et al., 2008, 2010).

TSS and CDOM showed a high sensitivity to band center with the best performing bands at the shortest wavelengths. Bands with centers longer than 685 nm tended to underperform the baseline at retrieving these components. This is an intuitive result as TSS and CDOM absorption both decrease with increasing wavelength leading to minimal information in the NIR region of the spectrum. For CDOM, the retrieval error for any red edge band is greater than any yellow band. For TSS, there is relatively minor improvement but only at wavelengths shorter than 685 nm around 695 nm.

The simultaneous addition of a yellow band and red edge band, shown in Fig. 7, outperformed the addition of either band individually. In Fig. 7, each of the 30 outlined boxes shown represent a different band combination, where each individual sub-element represents a different combination of widths. Wider bandwidths are placed lower in each box for the yellow band (y-axis), and further right for the red edge band (x-axis). For both bands, the HWHMs are defined to be 15, 18, 20, 25, and 30 nm. This means that the results generated using the two most narrow bands is always in the top-left of a box and those from the two widest bands are always in the bottom-right.

The two-band system retrieval error for all components is lower than that of the baseline for nearly all configurations. The only exception to this is the retrieval of CDOM by systems with yellow bands at 590 nm and red edge bands at longer wavelengths. These bands have previously been noted to lead to underperformance in CDOM retrieval when added individually. The best configuration for each individual component varies though they generally agree with what has been observed from the bands individually with Chl and PC. A 590 nm band paired with already well performing red edge led to the lowest Chl retrieval error despite the 590 nm band causing underperformance when added individually. Chl also saw the greatest decrease in retrieval error, outperforming the sole addition of yellow band retrieval regardless of band position or width. PC was retrieved equally well by a two-band system with yellow bands centered from 590 nm to 630 nm despite yellow bands at longer wavelengths showing worse performance when added alone. The change in Chl and PC retrieval performance for these noted bands may be a result of the spectral nature of IOPs and the LUT retrieval process. The addition of a single band can lead to an improvement in retrieval, but as the LUT retrieval process is essentially a spectral unmixing problem there is uncertainty in determining the extent that each component affects the newly sampled region. Changes in the spectrum by each component covary due to the spectral variation of IOPs, meaning that this uncertainty can be increased by sampling additional regions of the spectrum, leading to better a fit from the LUT and hence decreased retrieval error.

To summarize, the addition of a yellow and red edge band to the existing Landsat spectral coverage improves retrieval in most cases. Both the addition of only a yellow band or only a red edge band showed improvement in retrieval with some dependency on position and width. The addition of both bands simultaneously showed improvement nearly regardless of band position and width meaning that band configurations would be amenable to the needs of other application areas.

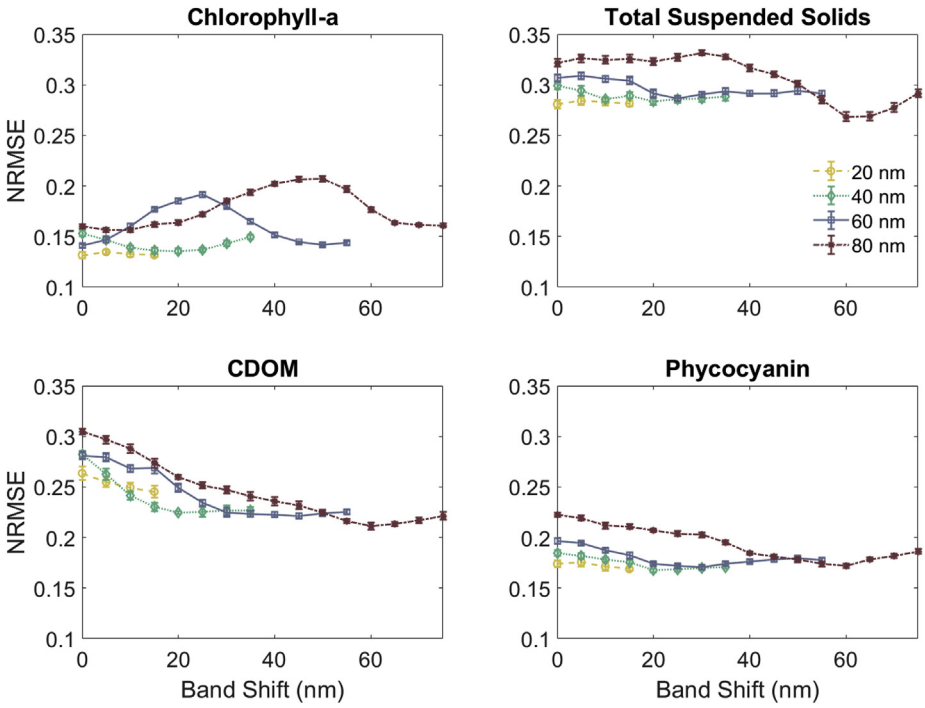

Fig. 9. Retrieval error of imaging spectrometers with band centers shifted until their positions repeated. Four spectrometer spacings were tested (20, 40, 60, and 80 nm). Each plot in this section is relates to the retrieval error of a different component.

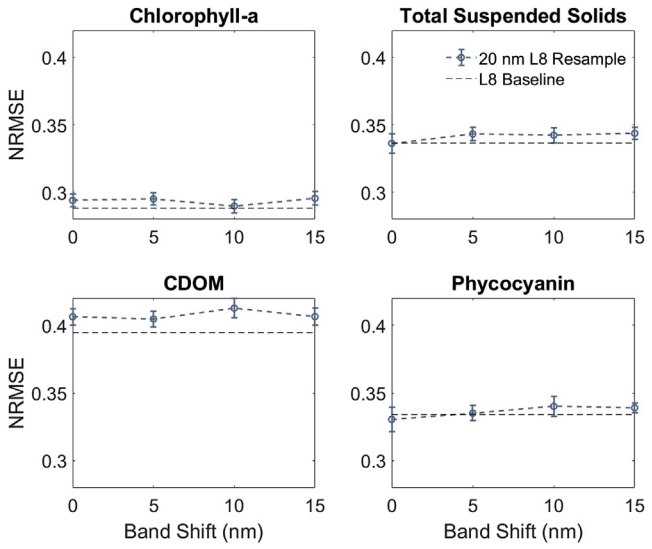

Fig. 10. Retrieval error of a 20 nm Imaging Spectrometer that has been resampled to the spectral coverage of Landsat 8. This resampling was tested on 4 different systems where the position of the band centers was shifted by increments of 5 nm, indicated by the x-axis. The dashed line indicates the performance of the baseline Landsat 8 model.

3.4. Performance of imaging spectrometers

In this section we show results for different imaging spectrometers spectral sampling configurations to allow for varying band center and bandwidth. Fig. 8 shows the effects of varying bandwidth on retrieval, Fig. 9 demonstrates the combined effect of shifting band centers and varying bandwidths on retrieval, and Fig. 10 tests data continuity through resampling of an imaging spectrometer with a 20 nm bandwidth to Landsat 8 RSRs.

The results of testing varying bandwidths show increasing retrieval error with increasing band spacing, as shown in Fig. 8. Recall that the shortest wavelength band is centered at 400 nm in each case. This is an intuitive result as wider bands average more spectral features when sampling the spectrum. Across all components, each modeled spectrometer had a retrieval error that was less than the baseline Landsat 8 model. This result may seem unexpected considering that a system with 100 nm increment spacing has only six bands in the 400 nm–900 nm range, compared to Landsat 8's five, but the spectrometer blankets this entire range while Landsat leaves considerable gaps (Fig. 1). Systems with a 60 nm or lower band spacing showed consistent retrieval error, with only small variations. A small upturn of retrieval error is noticeable for the 5 nm and 10 nm spectrometer, especially in the case of CDOM, which is most likely from increased noise due to smaller bandwidths. For spectrometers with spacings between 100 nm and 70 nm retrieval error was inconsistent. This may be due to the different band spacings changing the sampling of spectrum features leading to better or worse retrieval. This change in retrieval error suggests that a more optimal alignment of band sampling locations and features exists for wider spaced systems and was in part motivation for examining how shifting the spectrometer band center locations affected the performance of imaging spectrometers.

When testing shifting of imaging spectrometer band centers, systems with larger bandwidths had larger changes in retrieval depending on band shift, as shown in Fig. 9. Fig. 9 supports reasoning that the error in the wider spaced system was caused by the relative position of the band RSRs and spectrum features. The two systems most resilient to shifting were the ones with lower spacing, i.e. 20 nm and 40 nm, with the 20 nm system outperforming the 40 nm system. The 60 nm and 80 nm spectrometer show a notable decrease in retrieval error when shifted 40 nm and 60 nm, respectively, likely caused by both systems requiring an additional band to maintain full coverage of the entire 400 nm–900 nm range. These results indicate for a system with narrower bandwidths (e.g. 5, 10, 20 nm), band center locations are not critical. For potential systems with wider bandwidths band center location does impact retrieval of water constituents would need their positions considered. This is consistent with the results of Cao et al. (2019) which showed wider bandwidths decreased accuracy of various inland water remote sensing

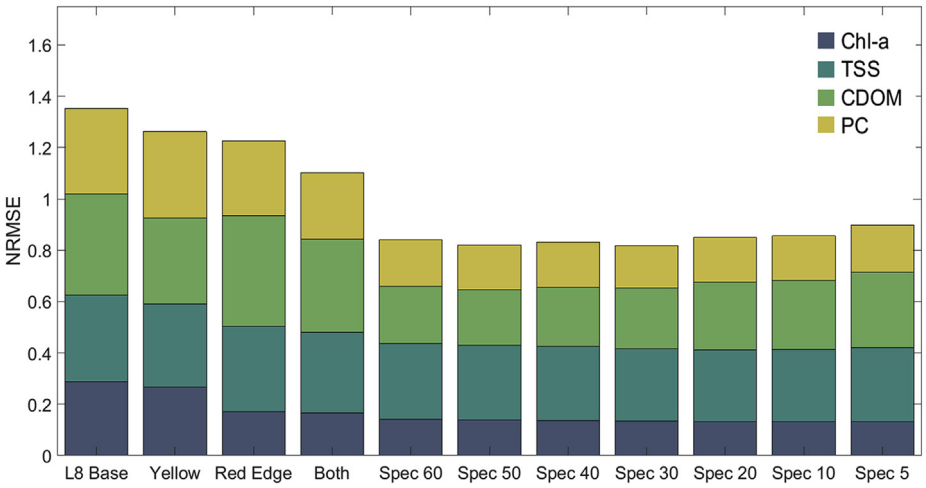

Fig. 11. Comparison of spectral coverages tested along with the baseline system. Multispectral systems are represented by the mean retrieval error over all centers and widths. The imaging spectrometers reported range in FWHM from 60 nm to 5 nm with centers shifted to the location of optimal performance.

algorithms.

The retrieval error of the resampled spectra with a 20 nm FWHM spectrometer, shown in Fig. 10, matches the retrieval of the base Landsat 8 system well, with little sensitivity to band shifting. The NRMSE difference between the baseline and resampled systems was less than 0.01 for almost all components except CDOM which was slightly higher around 0.01 to 0.02. Reconfiguring the spectrometer sampling to maximize the number of band centers that fall within the Landsat 8 band RSRs eliminates this difference. Similarly, performing the same test using a spectrometer with 10 nm spacing and no noise adjustment for bandwidth eliminates this difference as well. This indicates that retrieval ability of the resampled system is dependent on the relative placement of spectrometer band centers to the Landsat RSRs, inferring that spectrometers with narrower spacing are better suited for this task. Overall, these results show potential that spectrometer data can be resampled to maintain data continuity with Landsat 8 for water applications.

4. Conclusion

In this work, we perform modeling studies to determine how future Landsat systems could be improved for water quality monitoring. This testing focuses on determining how augmenting spectral sampling and resolution of Landsat systems impacts performance of an LUT spectral matching algorithm. Adding a single band to the existing Landsat 8 system showed improvement in retrieving all components (Fig. 11), both in the case of the Red Edge and Yellow band, though this was dependent on the band's placement and width. The best performing bands were generally those with smaller bandwidths. Simultaneously adding both bands not only lessened this dependency but allowed for a greater decrease in error. Retrieval error tended to decrease as spectral sampling and resolution increased over the visible/NIR region. This is reinforced by the modeled imaging spectrometer with 100 nm band spacing (i.e. 5 bands) that outperformed the Landsat 8 baseline model.

Our testing demonstrates the transition to a full imaging spectrometer for the VNIR portion of the spectrum for a future Landsat system will outperform the Landsat 8 baseline for water applications. The lowest retrieval error was achieved when the bands had an incremental spacing of about 30 nm. This spacing can be inferred to be the best trade-off between spectral resolution and the increased noise caused by the narrow bands and this configuration is insensitive to band center position. Our results also imply that resampling to a historic Landsat product is feasible with this spacing. The application of future Landsat missions for water quality monitoring will benefit from additional spectral sampling, regardless of the decision to implement a full imaging spectrometer or remain multispectral.

Future work should be supplemented by real world data. This could be done by implementation of multispectral and hyperspectral imaging systems on airborne platforms. This would allow better representation of how atmospheric compensation affects measured spectra. Further studies should also examine other attributes of a future Landsat system such as temporal revisit time which is critical for monitoring dynamic bloom events. The results of this study focus primarily on the use of Landsat for water quality monitoring, but similar modeling studies should be performed for other domains such as agriculture or forestry. These studies can allow the USGS and NASA to create meaningful design requirements for a system which performs optimally across applications.

Funding

The authors would like to thank the United States Geological Survey (USGS) for their initial funding (contract number G12PC00065) and sponsorship of this work.

Declaration of competing interest

The authors declare that they have no known competing financial interests or personal relationships that could have appeared to influence the work reported in this paper.

References

Aas, E., Høkedal, J., Sørensen, K., 2005. Spectral backscattering coefficient in coastal waters. Int. J. Rem. Sens. 26, 331–343.
Ahn, Y.-H., Bricaud, A., Morel, A., 1992. Light backscattering efficiency and related properties of some phytoplankters. Deep Sea Res. Part A. Oceanographic Res. Papers 39, 1835–1855.
Berk, A., Bernstein, L.S., Robertson, D.C., 1989. MODTRAN: A Moderate Resolution Model for LOWTRAN 7. Spectral Sciences, Inc.
Bricaud, A., Babin, M., Morel, A., Claustre, H., 1995. Variability in the chlorophyll-specific absorption coefficients of natural phytoplankton: analysis and parameterization. J. Geophys. Res.: Oceans 100, 13321–13332.
Bukata, R.P., Jerome, J.H., Kondratyev, K.Y., Pozdnyakov, D.V., 1991. Estimation of organic and inorganic matter in inland waters: optical cross sections of lakes Ontario and Ladoga. J. Great Lake. Res. 17, 461–469.
Cao, Z., Ma, R., Duan, H., Xue, K., 2019. Effects of broad bandwidth on the remote sensing of inland waters: implications for high spatial resolution satellite data applications. ISPRS J. Photogrammetry Remote Sens. 153, 110–122.
Carder, K.L., Chen, F.R., Cannizzaro, J.P., Campbell, J.W., Mitchell, B.G., 2004. Performance of the MODIS semi-analytical ocean color algorithm for chlorophyll-a. Adv. Space Res. 33, 1152–1159.
Concha, J.A., Schott, J.R., 2016. Retrieval of color producing agents in Case 2 waters using Landsat, 8 (185), 95–107.
Dekker, A., Pinnel, N., Gege, P., Briottet, X., Court, A., Peters, S., Turpie, K., Sterckx, S., Costa, M., Giardino, C., Braga, F., Bergeron, M., Heege, T., Pflug, B., 2018. Feasibility

Study of an Aquatic Ecosystem Earth Observing System. Committee on Earth Observation Satellites (CEOS), Australia.
Donlon, C., Berruti, B., Buongiorno, A., Ferreira, M.H., Féménias, P., Frerick, J., Goryl, P., Klein, U., Laur, H., Mavrocordatos, C., Nieke, J., Rebhan, H., Seitz, B., Stroede, J., Sciarra, R., 2012. The global monitoring for environment and security (GMES) sentinel-3 mission. Remote Sens. Environ. 120, 37–57.
EPA, National, 2017. Water Quality Inventory: Report to Congress. EPA/U.S. Environmental Protection Agency.
Fournier, G.R., Forand, J.L., 1994. Analytic phase function for ocean water. In: Ocean Optics, vol. XII, p. 2259.
Fujiki, T., Taguchi, S., 2002. Variability in chlorophyll a specific absorption coefficient in marine phytoplankton as a function of cell size and irradiance. J. Plankton Res. 24, 859–874.
Gerace, A.D., Schott, J.R., Nevins, R., 2013. Increased potential to monitor water quality in the near-shore environment with Landsat's next-generation satellite. J. Appl. Remote Sens. 7.
Gitelson, A.A., Schalles, J.F., Hladik, C.M., 2007. Remote chlorophyll-a retrieval in turbid, productive estuaries: chesapeake Bay case study. Remote Sens. Environ. 109, 464–472.
Gons, H.J., Rijkeboer, M., Ruddick, K.G., 2002. A chlorophyll-retrieval algorithm for satellite imagery (Medium Resolution Imaging Spectrometer) of inland and coastal waters. J. Plankton Res. 24, 947–951.
Gordon, H.R., Clark, D.K., Brown, J.W., Brown, O.B., Evans, R.H., Broenkow, W.W., 1983. Phytoplankton pigment concentrations in the Middle Atlantic Bight: comparison of ship determinations and CZCS estimates. Appl. Optic. 22, 20–36.
Hu, C., Lee, Z., Franz, B., 2012. Chlorophyll algorithms for oligotrophic oceans: a novel approach based on three-band reflectance difference. J. Geophys. Res.: Oceans 117.
IOCCG, 2012. Mission Requirements for Future Ocean-colour Sensors. International Ocean-Colour Coordinating Group, Dartmouth.
IOCCG, 2018. Earth Observations in Support of Global Water Quality Monitoring. International Ocean-Colour Coordinating Group, Dartmouth.
Johansen, R.A., Beck, R., Stumpf, R., Lekki, J., Tokars, R., Tolbert, C., McGhan, C., Black, T., Ma, O., Xu, M., Liu, H., Reif, M., Emery, E., 2019. HABSat-1: assessing the feasibility of using CubeSats for the detection of cyanobacterial harmful algal blooms in inland lakes and reservoirs. Lake Reservoir Manag. 35, 193–207.
Kuhn, C., Matos Valerio, A., Ward, N., Loken, L., Sawakuchi, H.O., Kampel, M., Richey, J., Stadler, P., Crawford, J., Striegl, R., Vermote, E., Pahlevan, N., Butman, D., 2019. Performance of Landsat-8 and Sentinel-2 surface reflectance products for river remote sensing retrievals of chlorophyll-a and turbidity. Remote Sens. Environ. 224, 104–118.
Kutser, T., Paavel, B., Verpoorter, C., Ligi, M., Soomets, T., Toming, K., Casal, G., 2016. Remote sensing of black lakes and using 810 nm reflectance peak for retrieving water quality parameters of optically complex waters. Rem. Sens. 8.
Lee, Z., Carder, K.L., Arnone, R.A., 2002. Deriving inherent optical properties from water color: a multiband quasi-analytical algorithm for optically deep waters. Appl. Optic. 41, 5755–5772.
Li, J., Yu, Q., Tian, Y.Q., Becker, B.L., Siqueira, P., Torbick, N., 2018. Spatio-temporal variations of CDOM in shallow inland waters from a semi-analytical inversion of Landsat-8. Remote Sens. Environ. 218, 189–200.
Lunettaa, R.S., Schaefferb, B.A., Stumpf, R.P., Keith, D., Jacobs, S.A., Murphy, M.S., 2015. Evaluation of cyanobacteria cell count detection derived from MERIS imagery across the eastern USA. Remote Sens. Environ. 157, 24–34.
Mathworks, Matlab documentaiton - lsqnonlin. https://www.mathworks.com/help/optim/ug/lsqnonlin.html, 2017 accessed 12 January 2017.
Mishra, S., Mishra, D.R., 2014. A novel remote sensing algorithm to quantify phycocyanin in cyanobacterial algal blooms. Environ. Res. Lett. 9.
Mishra, S., Mishra, D.R., Lee, L., Tucker, C.S., 2013. Quantifying cyanobacterial phycocyanin concentration in turbid productive waters: a quasi-analytical approach. Remote Sens. Environ. 133, 141–151.
Mitchell, G.B., Kiefer, D.A., 1988. Chlorophyll α specific absorption and fluorescence excitation spectra for light-limited phytoplankton. Deep Sea Res. Part A. Oceanographic Res. Papers 35, 639–663.
Mobley, C.D., Sundman, L.K., 2013. Hydrolight 5.2/Ecolight 5.2 Technical Documentation. Sequoia Scientific, Inc.
Mobley, C.D., Sundman, L.K., Davis, C.O., Bowles, J.H., Downes, T.V., Leathers, R.A., Montes, M.J., Bissett, W.P., Kohler, D.D.R., Reid, R.P., Louchard, E.M., Gleason, A., 2005. Interpretation of hyperspectral remote-sensing imagery by spectrum matching and look-up tables. Appl. Optic. 44 (Issue 17), 3576–3592.
Morel, A., 1974. Optical properties of pure water and pure sea water. In: Jerlov, N.G., Nielsen, E.S. (Eds.), Optical Aspects of Oceanography. Academic Press, New York, pp. 1–24.
Morfitt, R., Barsi, J., Levy, R., Markham, B., Micijevic, E., Ong, L., Scaramuzza, P., Vanderwerff, K., 2015. Landsat-8 operational land imager (OLI) radiometric performance on-orbit. Rem. Sens. 7, 2208–2237.
Mouw, C.B., Greb, S., Aurin, D., DiGiacomo, P.M., Lee, Z., Twardowski, M., Binding, C., Hu, C., Ma, R., Moore, T., Moses, W., Craig, S.E., 2015. Aquatic color radiometry remote sensing of coastal and inland waters: challenges and recommendations for future satellite missions. Remote Sens. Environ. 160, 15–30.
NGAC, Recommendations for Possible Future U.S., 2018. Global Land Data Collection Missions beyond Landsat 9. National Geospatial Advisory Committee.
Nguy-Robertson, A., Li, L., Tedesco, L.P., Wilson, J.S., Soyeux, E., 2013. Determination of absorption coefficients for chlorophyll a, phycocyanin, mineral matter and CDOM from three central Indiana reservoirs. J. Great Lake. Res. 39, 151–160.
Noaa, G.L.E.R.L., 2019. Archived Lake Erie water quality and microcystin data. https://www.glerl.noaa.gov/res/HABs_and_Hypoxia/wle-weekly/ accessed 8 December 2019.
O'Reilly, J.E., Maritorena, S., Mitchell, B.G., Siegel, D.A., Carder, K.L., Garver, S.A., Kahru, M., McClain, C., 1998. Ocean color chlorophyll algorithms for SeaWiFS. J. Geophys. Res.: Oceans 103, 24937–24953.
Pahlevan, N., Chittimalli, S.K., Balasubramanian, S.V., Vellucci, V., 2019. Sentinel-2/Landsat-8 product consistency and implications for monitoring aquatic systems. Remote Sens. Environ. 220, 19–29.
Palmer, S.C.J., Kutser, T., Hunter, P.D., 2015. Remote sensing of inland waters: challenges, progress and future directions. Remote Sens. Environ. 157, 1–8.
Palmer, S.C.J., Kutser, T., Hunter, P.D., 2015. Remote sensing of inland waters: challenges, progress and future directions. Remote Sens. Environ. 157, 1–8.
Petzold, T.J., 1972. Volume Scattering Functions for Selected Ocean Waters. Scripps Institution of Oceanography.
Pope, R.M., Fry, E.S., 1997. Absorption spectrum (380–700 nm) of pure water. II. Integrating cavity measurements. Appl. Optic. 36, 8710–8723.
Randolph, K., Wilson, J., Tedesco, L., Li, L., Pascual, D.L., Soyeux, E., 2008. Hyperspectral remote sensing of cyanobacteria in turbid productive water using optically active pigments, chlorophyll a and phycocyanin. Remote Sens. Environ. 112, 4009–4019.
Ruddick, K.G., Ovidio, F., Rijkeboer, M., 2000. Atmospheric correction of SeaWiFS imagery for turbid coastal and inland waters. Appl. Optic. 39, 897–912.
Sarada, R., Pillai, M.G., Ravishankar, G.A., 1999. Phycocyanin from Spirulina sp: influence of processing of biomass on phycocyanin yield, analysis of efficacy of extraction methods and stability studies on phycocyanin. Process Biochem. 34, 795–801.
Schalles, J.F., Yacobi, Y.Z., 2000. Remote detection and seasonal patterns of phycocyanin, carotenoid and chlorophyll pigments in eutrophic waters. Arch. Hydrobiol. Spec. Issues Adv. Limnol. 55, 153–168.
Simis, S.G.H., Peters, S.W.M., Gons, H.J., 2005. Remote sensing of the cyanobacterial pigment phycocyanin in turbid inland water. Limnol. Oceanogr. 50, 237–245.
Simis, S.G.H., Ruiz-Verdú, A., Domínguez-Gómez, J.A., Peña-Martinez, R., Peters, S.W.M., Gons, H.J., 2007. Influence of phytoplankton pigment composition on remote sensing of cyanobacterial biomass. Remote Sens. Environ. 106, 414–427.
Stramski, D., Babin, M., Woźniak, S.B., 2007. Variations in the optical properties of terrigenous mineral-rich particulate matter suspended in seawater. Limnol. Oceanogr. 52, 2418–2433.
Vander Woude, A., Ruberg, S., Johengen, T., Miller, R., Stuart, D., 2019. Spatial and temporal scales of variability of cyanobacteria harmful algal blooms from NOAA GLERL airborne hyperspectral imagery. J. Great Lake. Res. 45, 536–546.
Vanhellemont, Q., Ruddick, K., 2014. Turbid wakes associated with offshore wind turbines observed with Landsat 8. Remote Sens. Environ. 145, 105–115.
Vodacek, A., Blough, N.V., DeGrandpre, M.D., DeGrandpre, M.D., Nelson, R.K., 1997. Seasonal variation of CDOM and DOC in the middle Atlantic bight: terrestrial inputs and photooxidation. Limnol. Oceanogr. 42, 674–686.
Wu, Z., Snyder, G., Vadnais, C., Arora, R., Babcock, M., Stensaas, G., Doucette, P., Newman, T., 2019. User needs for future Landsat missions. Remote Sens. Environ. 231.
Wulder, M.A., Loveland, T.R., Roy, D.P., Crawford, C.J., Masek, J.G., Woodcock, C.E., Allen, R.G., Anderson, M.C., Belward, A.S., Cohen, W.B., Dwyer, J., Erb, A., Gao, F., Griffiths, P., Helder, D., Hermosilla, T., Hipple, J.D., Hostert, P., Hughes, M.J., Huntington, J., Johnson, D.M., Kennedy, R., Kilic, A., Li, Z., Lymburner, L., McCorkel, J., Pahlevan, N., Scambos, T.A., Schaaf, C., Schott, J.R., Sheng, Y., Storey, J., Vermote, E., Vogelmann, J., White, J.C., Wynne, R.H., Zhu, Z., 2019. Current status of Landsat program, science, and applications. Remote Sens. Environ. 225, 127–147.
Wynne, T.T., Stumpf, R.P., Tomlinson, M.C., Dyble, J., 2010. Characterizing a cyanobacterial bloom in Western Lake Erie using satellite imagery and meteorological data. Limnol. Oceanogr. 55, 2025–2036.
Wynne, T.T., Stumpf, R.P., Tomlinson, M.C., Warner, R.A., Tester, P.A., Dyble, J., Fahnenstiel, G.L., 2008. Relating spectral shape to cyanobacterial blooms in the Laurentian Great Lakes. Int. J. Rem. Sens. 29.
Yacobi, Y.Z., Köhler, J., Leunert, F., Gitelson, A., 2015. Phycocyanin-specific absorption coefficient: eliminating the effect of chlorophylls absorption. Limnol Oceanogr. Methods 13, 157–168.
Zheng, G., DiGiacomo, P.M., 2017. Uncertainties and applications of satellite-derived coastal water quality products. Prog. Oceanogr. 159, 45–72.